Smectic order-driven total wall defect formation

Luka Mesarec [a] , Jean de Dieu Niyonzima [b,c] , Haifa Jeridi [d] , Alina Vlad [e] ,
Alessandro Coati [e] , Michel Goldmann [b] , David Babonneau [f] , Doru Constantin [g] ,
Yves Garreau [e] , Bernard Croset [b] , Aleš Iglič [a] , Emmanuelle Lacaze [b] , Samo Kralj [h,i,*]

[a] Laboratory of Physics, Faculty of Electrical Engineering, University of Ljubljana, 1000 Ljubljana, Slovenia
[b] Sorbonne Université, CNRS, Institut des NanoSciences de Paris INSP, 75005 Paris, France
[c] Physics Department, School of Science, College of Science and Technology, University of Rwanda, Po.Box: 3900 Kigali, Rwanda
[d] OMNES Education Research center, ECE Paris, 37 quai de Grenelle, 75015 Paris, France
[e] Synchrotron SOLEIL, BP 48, L'Orme des Merisiers, 91192 Gif sur Yvette Cedex, France
[f] Université de Poitiers, ISAE-ENSMA, CNRS, PPRIME, Poitiers, France
[g] Université de Strasbourg, CNRS, Institut Charles, 67034 Strasbourg Cedex, France
[h] Department of Physics, Faculty of Natural Sciences and Mathematics, University of Maribor, 2000 Maribor, Slovenia
[i] Condensed Matter Physics Department, Jožef Stefan Institute, 1000 Ljubljana, Slovenia

ABSTRACT

We study experimentally and theoretically liquid crystal structure of smectic oily streaks, focusing on planar wall defects hosted within smectic flattened hemicylinders (SFHs). The wall configuration is singular both in orientational and translational order and we refer to it as the Total Wall Defect (TWD). Here "singular" refers to nematic director field and smectic phase field. In theoretical analysis of the TWD we use a mesoscopic Landau-de Gennes-Ginsburg approach in terms of the nematic tensor order parameter and smectic A (SmA) complex order parameter field. The smectic layer structure is experimentally determined using polarizing optical microscopy and X-ray diffraction measurements at Synchrotron facilities. We demonstrate theoretically and numerically that the experimentally observed abrupt change of the SmA layering in the centre of the wall defect is realized via nematic order reconstruction mechanism. Our experiments reveal that smectic layer spacing above and below the wall are almost similar. The theoretical analysis suggests that lateral SFH boundary conditions determine the vertical position of TWD.

1. Introduction

Interfaces and thin films formed by soft anisotropic materials [1–3] display a rich variety of different configurations, which are of interest for various applications and also for fundamental physics. Particularly complex patterns could emerge in the presence of geometrically imposed frustrations. These could stabilize topological defects (TDs) [4] enabling abrupt configurational changes on a short distance. In the present paper, we study such phenomena in geometrically frustrated thin smectic A (SmA) liquid crystal (LC) films.

SmA LCs represent one of the simplest LC phases simultaneously exhibiting liquid-like, orientational and translational order [5]. In a Landau-de Gennes-Ginsburg-type mesoscopic approach [6], the orientational order is given by the tensor nematic order parameter $\mathbf{Q}$. In a bulk equilibrium, the orientational order is uniaxial and spatially

homogenous. Furthermore, the system possesses a mass density spatial variation in the form of one-dimensional stack of equidistant layers, with translational order being characterized by the smectic complex order parameter ψ. The uniaxial orientational order is commonly expressed [6] as $\mathbf{Q} = s(\mathbf{n} \otimes \mathbf{n} - \mathbf{I}/3)$ in terms of the uniaxial scalar order parameter s and the nematic director field $\mathbf{n}$. Here s measures the amplitude of orientational order. The unit vector $\mathbf{n}$ points along the local axial direction, where the states $\pm \mathbf{n}$ are physically equivalent (the so-called head-to-tail invariance). On the other hand, the transitional order is mimicked by [6] $\psi = \eta e^{i\phi}$, where η measures the amplitude of layering and the smectic phase, ϕ, determines the location of smectic layers. In bulk equilibrium, s and η are spatially homogenous, $\mathbf{n}$ points along a single symmetry breaking direction, and $\phi = q_o \mathbf{n}.\mathbf{r}$. The wave vector $q_o = 2\pi/d_0$ determines the equilibrium smectic layer distance d_0.

If LC order is frustrated, topological defects could emerge both in

orientational and translational order. TDs [4,5,7] refer to localized distortions, where the relevant order is in general not uniquely defined. In nematic orientational order, point or line defects [5] are commonly observed and could be stabilized topologically. On the other hand, wall defects in orientational order, which play an important role in our study, could be stabilized only energetically [5]. For instance, nematic wall defect-like structure could be realized in severely confined LCs by locally entering biaxial states. A classic example corresponds to order-reconstruction (OR) nematic deformation [8] realized in strong spatial confinement [8–10] within a plan-parallel cell of thickness h imposing frustrating boundary conditions [8]. A typical geometrical setup in which OR nematic pattern could be realized is depicted in Fig. 1. In this setting one substrate enforces i) homeotropic anchoring, while another one enforces ii) tangential anchoring. Such boundary conditions enforce $\boldsymbol{n}$ to be locally aligned along the i) substrate surface normal and ii) perpendicular to it, respectively. In thick enough cells (with respect to the nematic biaxial order parameter correlation length ξ_b [8]), the nematic order within the cells is essentially uniaxial and $\boldsymbol{n}$ gradually reorients on traversing the cell to satisfy the conflicting boundary conditions, as depicted in Fig. 1a. For the cases where a similar orientational conflict is imposed on a distance comparable to ξ_b, the frustration is resolved via the OR mechanism [8–10] in which $\boldsymbol{Q}$ must enter biaxial states. The corresponding structural transformation is realized by the exchange [11] of $\boldsymbol{Q}$ eigenvalues, while the $\boldsymbol{Q}$ eigenvector frame remains fixed (Fig. 1b). This behavior is accompanied by $\boldsymbol{Q}$ eigenvalues spatial variations in two-dimensional nematic *amplitude* order parameter space (see Methods and Fig. 7). The key requirement for the OR activation is the presence of a large enough contradicting orientational order imposed on the length scale ξ_b. In this contribution, we show that a wall-like OR structure can be triggered also via the SmA order in hybrid-like confinements.

We consider the so-called smectic oily streaks [12–16], which can appear in free thin SmA films covering a flat substrate enforcing tangential order. In the case where SmA-air interface imposes homeotropic anchoring, the resulting antagonistic anchoring leads to the formation of periodic smectic flattened hemicylinders (SFHs), separated by grain boundaries, as schematically shown in Fig. 2a. Two quarter cylinders are formed at each edge of the SFHs [14]. The hallmark feature of SFHs are planar wall defects, at which smectic layer stacking suffers discontinuous reorientation (Fig. 2b) [14]. The structure of this wall

represents the open problem that we resolve in this paper. We show that the wall represents a Total Wall Defect (TWD) where both smectic and nematic order become frustrated, the latter exhibiting OR transformation.

2. Results

To understand the LC structural details of the wall defect embedded within the SFHs, we first present experimental measurements of oily streaks using Polarizing Optical Microscopy (POM) and X-ray diffraction. Then we reveal the LC configurational details using a mesoscopic Landau-de Gennes-Ginsburg approach using least possible algebra to describe the key structural features.

2.1. Experimental measurements

Smectic films of average thickness 180 nm have been prepared by depositing smectic 4-n-octyl-4′-cyanobiphenyl (8CB) on rubbed polyvinyl-alcohol (PVA) substrate that promote a planar unidirectional anchoring whereas air imposes homeotropic anchoring. The schematic presentation of the resulting oily streaks is given in Fig. 2a. Due to this hybrid anchoring, the smectic layers are curved in SFHs oriented along a single direction (Ox) perpendicular to the PVA substrate rubbing. These SFHs can be detected by POM in reflection between crossed polarizers (Fig. 2c). They are of width around 600 nm for a thickness 180 nm. Their internal structure has been extensively studied using combined X-ray diffraction and ellipsometry measurements [14,16]. As shown in Fig. 2b, which displays a side-view ((Oyz) plane) of one given hemicylinder, a sublayer of perpendicular smectic layers is formed at the basis of each SFH, covering all the PVA substrate, in line with a strong planar unidirectional anchoring. It is of thickness of the order of 20 - 30 nm [14]. A two-dimensional (2D) central defect (in green in Fig. 2b) of width around 400 nm is then created in the flattened hemicylinder centre on the top of the sublayer [14]. It connects the perpendicular layers in the sublayer and the parallel layers above the defect.

Using X-ray diffraction, we probe layers covering the substrate, including in particular the ones below the central defect. For such a purpose, we have firstly used a reflection set-up in Grazing Incidence where the X-ray beam is almost parallel to the 8CB hemicylinders, being only slightly tilted with respect to the SFHs by an out of plane incident
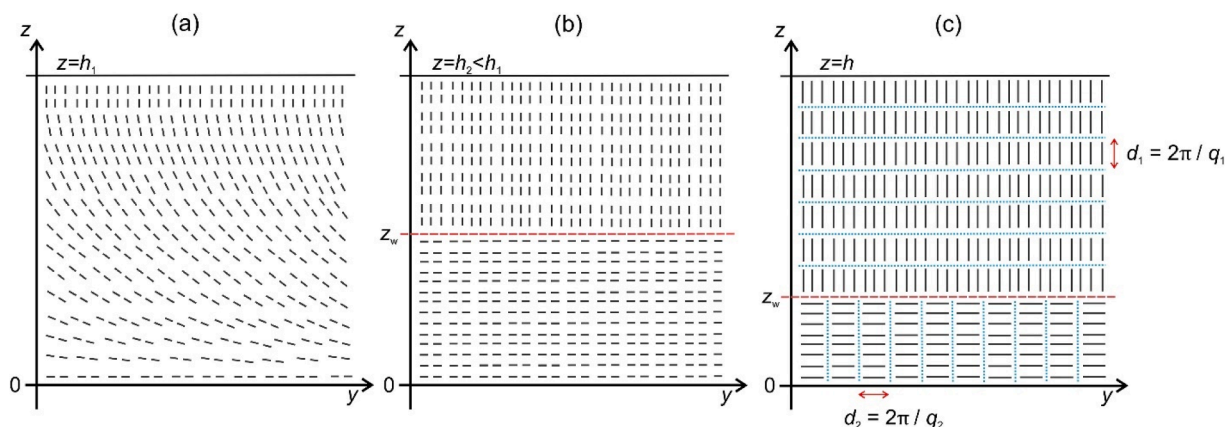
Fig. 1. Qualitatively different LC structures within a plane-parallel cell of thickness h enforcing hybrid orientational boundary conditions: homogeneous tangential along the y-axis at $z = 0$ and homeotropic at $z = h$. a) In the nematic phase, a non-singular "escaped" solution is formed if $h = h_1$ is larger than the biaxial coherence length ξ_b. The nematic order within this structure is essentially uniaxial and can be well presented by the nematic director field. The lines represent a typical orientational order for such cases. b) Schematic presentation of nematic LC order within a cell in which the imposed frustration in orientational order is resolved via the OR mechanism. The shown orientational order depicts orientations of the principal Q eigenvector. The imposed orientational frustration is resolved by forming a wall defect at $z = z_w$, which requires entering biaxial states. More detailed changes across the wall are depicted in Figs. 7 in Methods. In the nematic phase, such structure is possible only if $h = h_2 \sim \xi_b$, i.e., $h_2 \ll h_1$. c) The case where SmA layers are formed (they are indicated by dotted lines). These layers suppress the nematic bend deformation if the smectic order is strong enough. In this case OR could be realized also in thicker cells (e.g., $h \gg \xi_b$). The smectic layer period d above (d_1) and below (d_2) the wall could be different.
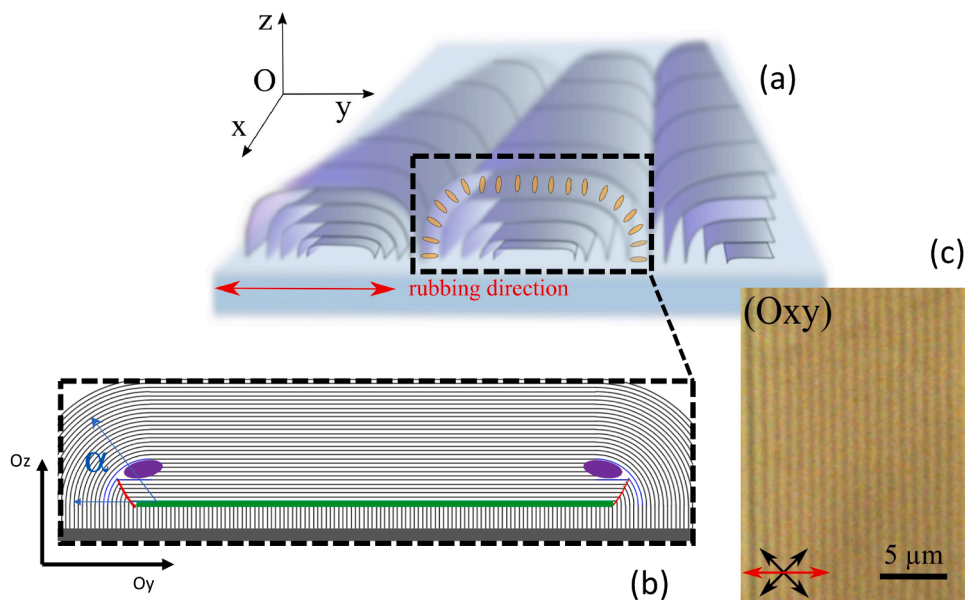
Fig. 2. a) Simplified 3D schematics of the oily streaks where smectic layers are curved in flattened hemicylinders, with the molecular orientation shown in yellow. b) Cross-sectional views ((Oyz) plane) of one given hemicylinder for a film height of 180 nm. In contrast with the schematics of Fig. 2a, all layers are shown including the perpendicular layers at the proximity of the substrate. Two rotating grain boundaries in red terminated by a dislocation in purple are expected close to the centre of curvature of the curved smectic layers at the edges of the hemicylinders. The 2D central defect in the centre of the hemicylinders is shown in green. c) The POM picture in reflection shows the top view of oily streaks ((Oxy) plane) for an 8CB film thickness around 200 nm, with each stripe corresponding to one hemicylinder.

angle ω that has been varied between 0.15° and 0.6° (see Methods). For all ω values, a scattering ring is observed in the (q_y, q_z) plane of the reciprocal space as shown on Fig. 3a. If the Bragg conditions are fulfilled, which is provided using two incident angles (see Methods), the position of the scattered ring defines the wave-vector transfer q of the absolute value $q = 2\pi/d$, where d is the average smectic layers spacing for layers of normal parallel to q. The q orientation along the ring is determined by the angle α (Fig. 3a) with the ring intensity for a given α being thus associated with the smectic layers oriented with their normal at α with respect to the substrate (Fig. 2b). The ring intensity and position have been measured from α around 15° (at the basis of the circle, associated with smectic layers almost perpendicular to the substrate) to α around 90° (at the top of the circle, associated with smectic layers parallel to the substrate, see Methods). The observation of a continuous scattered ring (Fig. 3a) confirms a structure similar to the one shown on Fig. 2b for the edges of the SFHs where the orientation of the smectic layers

continuously varies. The increase of intensity when α reaches 90° (Methods – see Fig. 6) confirms the presence of a large zone of straight smectic layers, almost parallel to the substrate, in the centre of the SFHs on top of the central defect in green in Fig. 2b Around 90° the signal is thus dominated by the straight central smectic layers. The q curve obtained in Bragg conditions (see Methods) as a function of α has been accordingly extracted from $\alpha \sim 15°$ to $\alpha \sim 90°$ (Fig. 3b - see Methods). Due to refraction effects, values for α smaller than around 15° could not be obtained (see Methods). To complement the $q(\alpha)$ curve from $\alpha = 0°$ to $\alpha = 12°$, TSAXS measurements have been conducted where the sample is now almost perpendicular to the X-ray beam, i.e. $\omega = 90°$, while being slightly rotated around the Ox axis by 16° (see Methods).

The complete $q(\alpha)$ curve obtained in Bragg conditions is shown on Fig. 3b It is divided into three main parts. The first part around $\alpha \sim 90°$ corresponds to the central smectic layers on top of the central defect. The central layers being confined between the central defect and air are
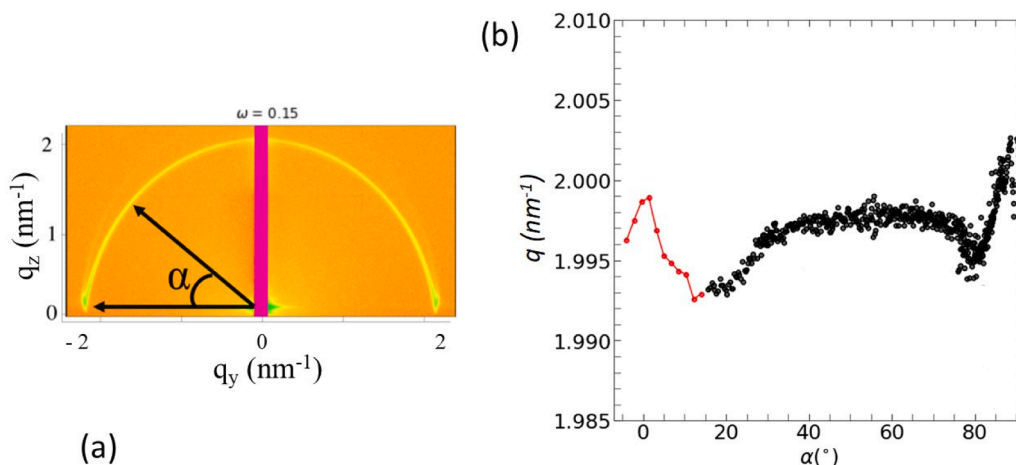
Fig. 3. a) 2D X-ray diffraction pattern for an incident angle $\omega = 0.15°$ and a detector dead zone centred on the top of the ring (see section Methods) b) Evolution of the wave-vector transfer value q in Bragg condition when the orientation of the wave-vector transfer q varies over 93° in overall. Red and black symbols correspond to data from TSAXS and GISAXS measurements, respectively.

expected to present a non-modified layer spacing that may be the natural 8CB period ($d_0 = 2\pi / q_0$). Indeed $q_0 = 2.003 \pm 0.001$ nm^{-1} is close to the already published values for q_0 around 2 nm^{-1} [17,18]. The second part between $\alpha = 85°$ and $\alpha = 10°$ corresponds to the rotating smectic layers at the edge of the SFHs. The data indicate that the rotating layers are dilated, as shown by the average q values being consistently lower than q_0 for all α (consequently, the layer spacing d is larger than d_0). This observed dilation of the rotating layers associated with average d values ~0.25 % smaller than d_0 may be the result of the extremely large bending energy of the smectic layers of small radius of curvature shown in Fig. 2b at the edge of the SFHs. Dilation of rotating smectic layers indeed allows to increase the curvature radius. Since the perpendicular layers below the rotating layers can be viewed as a continuation of these rotating layers when α decreases towards 0°, we can consider that their average q value, $q_{\perp,1}$, is almost the one measured at $\alpha = 15°$, $q_{\perp,1} = 1.992 \pm 0.001$ nm^{-1}. The third part of the curve in Fig. 3b around $\alpha = 0°$ corresponds to the average q value of all smectic layers perpendicular to the substrate $q_\perp = 1.999 \pm 0.001$ nm^{-1}. Two families of perpendicular smectic layers are expected. The first one corresponds to the perpendicular smectic layers at the edges of the SFHs, below the rotating smectic layers, which average value is $q_{\perp,1}$. The second family is below the central defect with its average $q_{\perp,2}$. The fact that the average $q_\perp$ for the two families is $q_\perp = 1.999 \pm 0.001$ nm^{-1}, which is larger than $q_{\perp,1}$, shows that $q_{\perp,2}$ is significantly larger than $q_{\perp,1}$. Considering that the width of an entire flattened hemicylinder for a thickness 180 nm is 570 nm [14], we obtain an overall number of perpendicular smectic layers of about 184. Further considering that the width of the central defect is around 400 nm [14], we obtain a number of perpendicular layers below the central defect of about 130. We consequently estimate 72 % of perpendicular layers below the central defects and 28 % below the rotating layers. $q_{\perp,2}$ can thus be estimated: $q_{\perp,2} = 1/0.72\,(q_\perp - 0.28\,q_{\perp,1})$ = 2.0017 ± 0.001 nm^{-1}. It is very close to q_0, suggesting that below and above the central defect, smectic layers possess similar layer spacings d_1 and d_2 (see Fig. 1c) that differ by <0.05 %. This is consistent with the sample preparation that doesn't imply any memory effect due to the substrate, where each 8CB film is being deposited on a freshly rubbed PVA substrate.

2.2. Total wall defect structure

The experimental results presented above combined with the previous studies [14] suggest that the smectic layers exhibit a discontinuous smectic layer rearrangement at the distance $z = z_w \approx 20 - 30$ nm, where the wall defect is localized. So far, a consistent theoretical model of the wall structure is absent, and the main aim of our study is to clarify its structure at the mesoscopic level. Below we show that this singularity represents a "total defect", which is singular both in orientational and translational order parameter fields, which are used to describe the bulk equilibrium order. We show that the orientational frustration is resolved via the order reconstruction mechanism and that its stability is enabled via SmA order.

To describe the wall LC structures, we use a Landau-de Gennes-Ginsburg – type phenomenological model in terms of nematic tensor order parameter $\mathbf{Q}$ (Eq. (5) in Methods) combined with smectic complex order parameter ψ (Eq. (9) in Methods). The structural changes are mainly enabled by spatial variations in the *amplitudes* of the order parameters. The nematic tensor $\mathbf{Q}$ is traceless, while the space of the $\mathbf{Q}$ *amplitude* parameters is two-dimensional. We describe the two variables as s_0 and γ (see Methods, Eqs. (7)). Here s_0 measures the effective nematic *amplitude* and γ measures the degree of biaxiality. The latter is also commonly measured by the biaxial parameter [19,20]

$$\beta^2 = 1 - \frac{6\left(Tr\mathbf{Q}^3\right)^2}{\left(Tr\mathbf{Q}^2\right)^3} = sin^2(3\gamma) \in [0,1]. \tag{1}$$

Nematic uniaxial states are determined by $\beta^2 = 0$. Biaxiality is

fingerprinted in $\beta^2 > 0$, where $\beta^2 = 1$ corresponds to the maximal degree of biaxiality. The space of the smectic *amplitude* order parameter is one-dimensional, given by $\eta = |\psi|$. The geometry of the problem and key structural features of the system are depicted in Fig. 1c and in Methods (Fig. 7) using Cartesian coordinates (x,y,z). To illustrate the phenomena of interest, we use the simplest possible geometrical setup which captures the essential physics. We set that the LC body is confined within a plane-parallel cell of thickness h. At $z = 0$ we impose strong uniaxial tangential anchoring along the y-axis, while at $z = h$ uniaxial homeotropic anchoring condition is imposed. These anchoring conditions mimic our experimental sample (i.e., substrate-LC interaction at $z = 0$ and air-LC interaction at the free LC surface) quite well when only the centre of the SFHs shown on Fig. 2a and b is considered. To accordingly consider flat interfaces, we can assume that the *amplitudes* of order parameters exhibit variations only along the z-axis, therefore not considering curvature of the smectic layers at the two extremities of the wall defect.

In agreement with the previously published combined X-ray diffraction – ellipsometry measurements [14], we assume that the SmA layer stacking exhibits discontinuous reorientation at the wall located at the distance z_w (scheme sketched in Fig. 1c). Below and above the wall, the smectic layers run along the y-axis and z-axis, respectively. Smectic configurations associated with the structures similar to the ones of our system were studied in [21]. The authors have formulated a model that is amenable to finite element simulations. They calculated that the same boundary conditions as the ones used in our study can be resolved by introducing edge disclinations at the edges of the hemicylinder. Such a configuration is not of the same thickness but similar to the structure that we propose in Fig. 2b for the centre of the hemicylinders (perpendicular smectic layers directly connected to each other in a planar defect). However, they did not study the biaxiality features of their structure. We believe that in their structure, biaxiality associated with OR is also present, which is the subject of our study.

The amplitude of translational order η must be melted at $z = z_w$ (i.e., $\eta(z_w) = 0$) to reconcile the different stacking of smectic layers above and below z_w. This abrupt change in smectic translational order also imposes severe frustration on orientational LC order. It enforces abrupt change in orientation of the nematic order occurring on a length scale equal to ξ_s - the smectic order parameter correlation length that is in the nanometer range. This can only be achieved either via order-reconstruction (OR) or by locally melting the nematic order. The latter mechanism is too costly because room temperature for 8CB is far below the isotropic-nematic transition. Therefore, the only option is the transformation of local LC order involving the OR mechanism [8–11]. In this structure, the nematic order enters biaxial states which mediate the conflicting orientational order enforced above and below z_w. The nematic structural transformation is realized without $\mathbf{Q}$ eigen frame rotation. The resulting qualitative changes in mesoscopic orientational order on traversing the wall at z_w are depicted in detail in Fig. 7a (mesoscopic shape variations) and Fig. 7b (degree of biaxiality) in Methods.

These configurational changes could be predicted by mapping structural variations in real space to the nematic *amplitude* order parameter space, shown in Fig. 7c in Methods. The corresponding points in real (Fig. 7a and b) and 2D amplitude order parameter space (Fig. 7c) are labelled with the numbers 1–5. The initial (1) nematic state at $z = 0$ is positively uniaxial along the y-axis (which is reflected in the prolate mesoscopic molecular shape) until $z = z_w - \Delta h$, corresponding to $\gamma = 0$. Δh is the defect thickness which is different from the sample thickness h shown in Fig. 1c. On increasing z above $z = z_w - \Delta h$, biaxial states are entered, and at (3), the negative uniaxial order (resulting in cylindrically symmetric oblate mesoscopic molecular shape) is realized along the x-axis, described by $\gamma = \pi/3$. Finally, on further increasing z (5), positive uniaxial order is reached between $z = z_w + \Delta h$ and $z = h$, for which $\gamma = 2\pi/3$. Topology implies that in between uniaxial configurations 1, 3, and 5, other zones exhibiting maximal biaxiality are reached (labelled with 2 and 4 on Fig. 7). Therefore, the finite structure of the TWD shown in

Fig. 7b consists of a negatively uniaxial sheet placed at z_w, which is further enclosed between two parallel sheets exhibiting maximal biaxiality. Note that uniaxial order at the confining plates located at $z = 0$ and $z = h$ is assumed to be realized by strong enough uniaxial orientational anchoring conditions (enforcing $\beta^2(0) = \beta^2(h) = 0$). To allow for the 90° reorientation of smectic layers on crossing the wall, the smectic order must be locally melted. Therefore, we request $\eta(z_w) = 0$. The resulting structure is singular both in the nematic director field and smectic phase field representation, which are used to describe bulk equilibrium nematic and SmA order, respectively. Consequently, we refer to this structure as the Total Wall Defect (TWD).

To study the essential features of the TWD numerically, we used the minimal model that still contains the key ingredients of the phenomena of our interest. We expressed the free energy of our model in terms of characteristic liquid crystal lengths (see Eqs. (13)). Furthermore, we used approximations which are correct deep in the SmA phase, in other words at the room temperature for the 8CB, for which the system's order can be described using only two variational parameters (instead of the usual description in terms of Q and ψ that requires seven independent parameters).

In the order reconstruction mechanism, the **Q** frame remains fixed, and the resulting configurational changes take place solely in the 2D nematic *amplitude* order parameter space. We use the Lyuksyutov constraint [22,23] (see Methods), according to which s_0 is spatially constant. This approximation relies on the weakly 1st order character of the I-N phase transition. Consequently, the cubic term in the nematic condensation free energy contribution is expected to be relatively small with respect to quadratic and quartic contributions deep in the nematic phase. If one neglects the cubic term one can minimize the condensation free energy contribution also by biaxial states. Consequently, in our geometrical setup the nematic *amplitude* field states could be described by the amplitude variational angle $\gamma = \gamma(z)$ only (see Eq. (7a) in Methods). Furthermore, we express the smectic order parameter as following:

$$\psi(z < z_w) = \eta(z)e^{iq_2 X}, \;\; \psi(z > z_w) = \eta(z)e^{iq_1 z}. \tag{2}$$

Here we allow the smectic layer spacing above $(d_1 = 2\pi/q_1)$ and below the wall $(d_2 = 2\pi/q_2)$ to be different (Fig. 1c).

The TWD structure is finally determined by the following variational parameters: $\gamma(z)$ that describes the nematic biaxiality and $\eta(z)$ which represents the smectic amplitude of translational order. The corresponding bulk free energy density reads (see Methods)

$$\frac{f}{Ls_0^2/d_0^2} = \frac{d_0^2}{\xi_b^2}g_c^{(n)} + g_e^{(n)} + \frac{1}{q_0^2\lambda^2}\left(\frac{d_0^2}{\xi_s^2}g_c^{(s)} + g_e^{(s)}\right), \tag{3}$$

$$g_c^{(n)} = \frac{1 - \cos(3\gamma)}{27}, \tag{3a}$$

$$g_e^{(n)} = \frac{2}{3}\left(\frac{\partial\gamma}{\partial\tilde{z}}\right)^2, \tag{3b}$$

$$g_c^{(s)} = -r\,\tilde{\eta}^2 + \frac{\tilde{\eta}^4}{2}, \tag{3c}$$

$$g_e^{(s)} = \left(\frac{\partial\tilde{\eta}}{\partial\tilde{z}}\right)^2 + 4\pi^2\varepsilon^2\tilde{\eta}^2, \tag{3d}$$

where $\tilde{\eta} = \frac{\eta}{\eta_0} \in [0,1]$ is the scaled smectic order parameter, r is the dimensionless temperature and $\tilde{z} = \frac{z}{d_0} \in [0,1]$ is the dimensionless spatial coordinate. L is the representative nematic elastic constant and s_0 the nematic amplitude (section Method – Eq. (11b)). The LC material properties are written in terms of material dependent lengths $d_0 = 2\pi/q_0$, the smectic natural 8CB period, ξ_b, ξ_s and λ. Here ξ_b stands for the biaxial nematic order parameter correlation length, ξ_s for the smectic order

parameter correlation length and λ for the smectic penetration length. These last three lengths depend on temperature and are directly related to the material constants as shown in the section Methods (Eq. (13)) [21, 24]. It is known that deep in the smectic phase, which corresponds to 8CB at room temperature, ξ_s and λ values are very close to d_0 [6]. Deep in the smectic phase, ξ_b is also on the nanometer range. We have thus considered in the following all lengths to be equal to d_0 which equals 3.14 nm.

The nematic condensation term $g_c^{(n)}$ enforces the nematic uniaxial order (and thus penalizes the biaxiality). The nematic elastic term $g_e^{(n)}$ favours spatially homogeneous nematic order. The smectic condensation term $g_c^{(s)}$ enforces smectic order for $r > 0$. The smectic elastic penalty $g_e^{(s)}$ consists of two different contributions; the 1st term favours spatially homogeneous smectic order parameter, while the second term penalizes dilatation or compression of smectic layers with respect to equilibrium. The resulting stress is thus described by the dimensionless stress

$$\varepsilon(z < z_w) = 1 - \frac{q_2}{q_0} \tag{4a}$$

and

$$\varepsilon(z > z_w) = 1 - \frac{q_1}{q_0}. \tag{4b}$$

We determined the variational parameters $\gamma(z)$ and $\eta(z)$ by numerically solving the Euler-Lagrange equations associated with the minimization of the overall free energy. The solution obeys the following boundary conditions: $\gamma(z = 0) = 0$, $\gamma(z = z_w) = \frac{\pi}{3}$, $\gamma(z = h) = 2\pi/3$, $\tilde{\eta}(z = 0) = \tilde{\eta}(z = h) = 1$, $\tilde{\eta}(z = z_w) = 0$. For simplicity, we assumed that both confining surfaces enforce the equilibrium value of η (i.e., $\gamma = 0$ and $\tilde{\eta} = 1$).

In the simulations we consider conditions which mimic experimental measurements focusing on the region containing the TWD. We measure all characteristic lengths in units of bulk smectic layer width, which we set to d_0=3.14 nm ($q_0 = 2.003$ nm^{-1}). We impose the cell height to $\frac{h}{d_0} = 57$ to match typical experimental case, i.e. $h \sim$180 nm. We assume that the layers above z_w are not dilated or compressed due to the "adaptable" LC-air limiting interface at $z = h$. In the region below z_w, we impose only a small compressibility free energy penalty, since the experimental measurements suggest that $\varepsilon(z < z_w) \le 0.0005$. We have thus chosen $\varepsilon(z < z_w) = 0.0005$.

The structure shown in Fig. 4a was obtained by minimizing the free energy of the system with respect to z_w. We show both the variations of the smectic parameter η and of the biaxial parameter γ as a function of z. The variation of the integrated free energy density is also shown on varying the position of TDW. It exhibits the minimum when z_w is placed roughly at the centre of the cell.

We first discuss the wall defect core structure. The core size of TWD, where LC structure essentially departs from bulk LC behaviour, extends roughly over the distance $\Delta h \approx 10$ associated with around 10 smectic layers, corresponding to roughly 30 nm. The length scales over which the amplitudes of nematic and smectic order are perturbed are comparable. They correspond to 10 smectic layers but also to ten times ξ_b. Right at the TWD centre ($z = z_w$), the smectic order parameter is melted ($\eta = 0$) and the nematic order parameter is negatively uniaxial $\left(\gamma = \frac{\pi}{3}\right)$. In the inset, we plot the degree of biaxiality which reveals where the two walls exhibiting maximal biaxiality are placed. The simulations suggest that they are placed symmetrically, few smectic layers above and below z_w.

We next focus on the position of TWD. The free energy curve in Fig. 4b shows that the energy minimum corresponds to a TDW at the centre of the cell. However, the zoom on the almost flat part of the curve shows that a localization of TDW at around $10d_0$, as experimentally observed, only requires a moderate increase of the free energy, i.e. only 0.12 % of ΔF_0. We consequently expect easy modifications of the TDW position with respect to a localization in the centre and a position of the
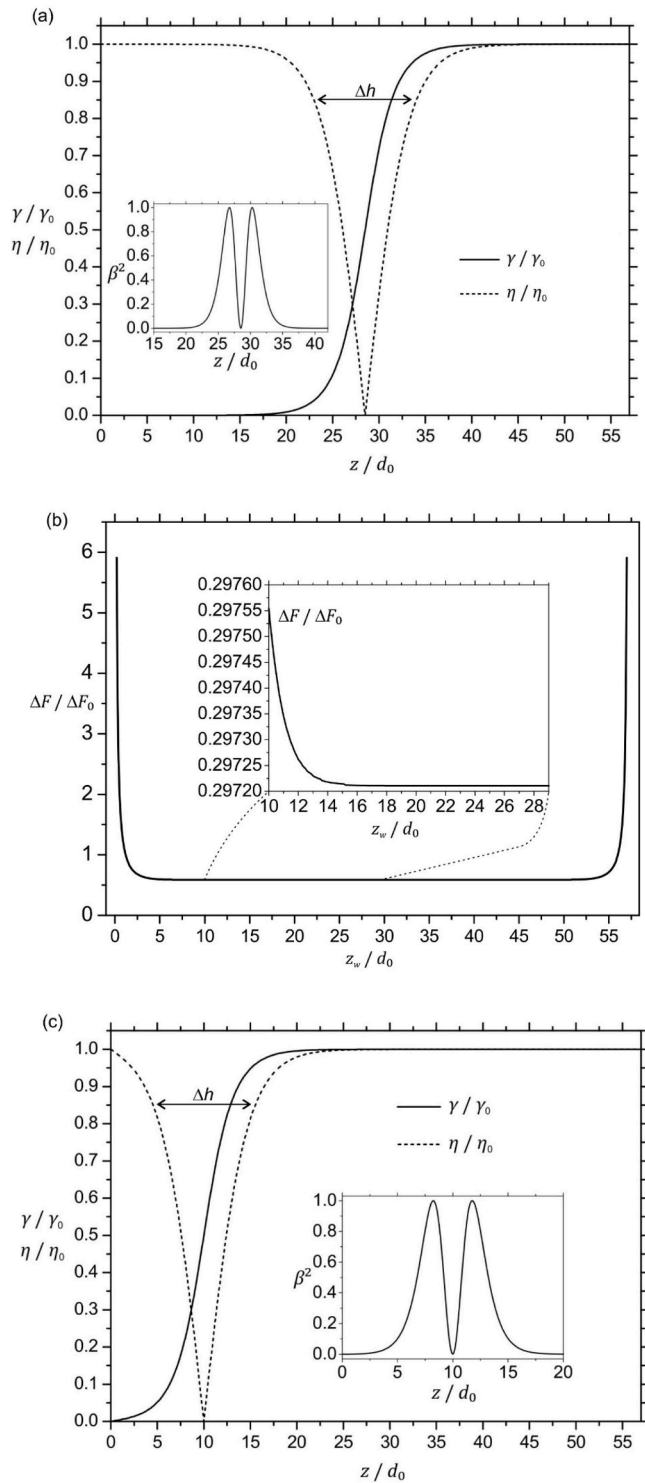
Fig. 4. Key features of nematic and SmA order on crossing the wall defect. At the wall centre, the smectic order is melted and the nematic order exhibits negative uniaxiality. In all cases we impose $\xi_b = \xi_s = d_0$, $r = 0.1$, $\varepsilon(z < z_w) = 0.0005$, $\varepsilon(z > z_w) = 0$, $h/d_0 = 57$, $d_0 = 3$ nm, $\lambda = d_0$. a) $z_w \sim h/2$. b) the excess free energy penalty $\Delta F = \int_0^h \left(f_e^{(n)} + f_e^{(s)} \right) dz$ in units of $\Delta F_0 = L s_0^2/d_0$ (see Eq. (3)). c) $\frac{z_w}{d_0} = 10$. In a) the wall position is determined via the free energy minimization.

wall defect that may strongly depend on the details at its lateral boundaries. We have thus calculated the structure shown in Fig. 4c that was obtained by imposing numerically $z_w = 10do$, as suggested experimentally. Comparison of configurations shown in Fig. 4a and c reveals that the resulting TWD core structures are essentially the same.

3. Discussion

We studied experimentally and theoretically wall defect-like configuration within smectic flattened hemicylinders (SFHs). Our combined Optical Microscopy and X-ray synchrotron measurements suggest that the defect of width ~ 400 nm is placed at $z_w \sim 20$–30 nm above the PVA substrate. The smectic layers below ($z < z_w$) and above ($z > z_w$) the wall are running in perpendicular directions, i.e., along the y-axis and z-axis of our laboratory coordinate system. Both layer spacings are very close from each other and very close to the natural 8CB period of 3.14 nm. Recently, the smectic layer structure has been calculated for similar thicknesses and boundary conditions [21]. With our model we have analysed the corresponding biaxiality parameters to reveal that a Total Wall Defect (TWD) is formed. The wall structure resolves contradicting imposed orientational order of smectic layers above and below the wall via order reconstruction (OR)-type mechanism on a distance that is of the order of $10\xi_b$, ξ_b being the biaxial nematic order parameter correlation length. So far OR walls have been reported only in nematic LCs in confining geometries [8–10] with imposed contradicting boundary conditions on a distance comparable to ξ_b or in strong external electric fields [25,26], whose characteristic field coherence length is comparable to ξ_b. The latter realization is similar to the OR-based mechanism that we report in the present paper. Namely, SmA layers locally act like an external ordering field, which tends to align LC molecules along a local layer normal. On crossing TWD at $z = z_w$, this effective ordering field exhibits on average a $90°$ change on a distance that is a few ξ_b if ξ_b is taken as equal to λ. In the centre of the TWD core, the smectic order vanishes, and the nematic order parameter is negatively uniaxial. Two walls exhibiting maximal biaxiality and relatively weak smectic order are placed symmetrically, a few smectic layers above and below z_w. We measured with unprecedented precision the average layer spacing below and above the wall and we found their values to be very similar. Our modelling with this very similar layer spacing above and below the wall predicts a localization of the TWD in the middle of the smectic film. However, our modelling also shows that only small free energy variations are required to localize the TDW close to the substrate, which is in agreement with our observations. This shows that the observed TDW localization might be imposed by the edges of the SFHs which are not considered in our model. We will focus on this issue in the near future.

Note that it is established that the OR solution is very robust [8]. Namely, in severe confinements, where the nematic order needs to reorient perpendicularly on the scale comparable to the biaxial correlation length, the solution of the classical bend-like reorientation of the order does not exist [8]. Therefore, if the perpendicular boundary condition on the scale comparable to ξ_b is imposed and if **Q** is allowed to enter biaxial states, only the OR solution exists deep in the nematic phase (which is fulfilled in our study where the system exhibits SmA order). We stress that strong elastic distortions within cores of common nematic line [10,11,22] and point defects [22] are commonly mediated via the OR mechanism. Our study illustrates that OR can also occur in smectic wall defects that join perpendicular layers due to the severe frustration on orientational LC order induced by the abrupt change in smectic translational order.

Understanding structural details of smectic oily streaks is useful for various applications in which LC medium is exploited for the trapping of different nanoparticles (NPs) to the desired regions where they could assemble into different patterns. Namely, cores of TDs efficiently trap NPs of appropriate size and surface treatment [27–29]. It has been shown that nanospheres of a 5 nm diameter form flat hexagonal monolayers in the TDW strictly oriented by the smectic layers below the

TDW [30,31]. To understand the interactions responsible for this orientation promising to control the optical properties of assemblies of nanoparticles, the knowledge of the TDW is a prerequisite. The understanding of how it varies in the presence of nanoparticles will the focus of our further investigations.

4. Materials and methods 1: experimental measurements

4.1. Sample preparation

Smectic films of average thickness 180 nm have been prepared by depositing smectic 4-n-octyl-4′-cyanobiphenyl (8CB) on rubbed polyvinyl-alcohol (PVA). The PVA of thickness around 10 nm has been prepared by spin coating a droplet (100 μL) of a 0.5 wt % aqueous solution of PVA from Sigma Aldrich with acceleration 400 rpm s^{-1}, speed 3000 rpm during 30 s on previously accurately cleaned glass slides (thickness 130 μm). Spin-coating has been used for the deposition of 8CB. 8CB from Sigma-Aldrich has been dissolved in toluene (0.2M). A droplet of 50 μL has then been deposited on the PVA once PVA has been rubbed with a rubbing machine and has been spincoated with a speed 3000 rpm, an acceleration between 500 rpm s^{-1} and 1000 rpm s^{-1} during 30 s.

4.2. X-ray diffraction measurements

At SOLEIL Synchrotron there is no DOI associated with the data. The data are consequently available upon request. X-ray diffraction measurements were carried out at the SIXS beamline of the SOLEIL synchrotron facility. The photon energy was fixed at 18.44 keV and the X-ray beam size was set at 300 μm × 100 μm. The scattering signal was collected on a 2D EIGER 1 M hybrid pixel detector (DECTRIS), which is located 1700 mm away from the sample. The experimental reflection and transmission set-ups are shown in Fig. 5. In a reflection set-up (Fig. 5a), the stripes observed by optical microscopy (Fig. 2c) are oriented almost parallel to the incident beam (Fig. 5a). The beam probes an area of width 300 μm and length of 18 mm, equal to the sample length. The scattered ring of Fig. 5a / Fig. 3a displays the scattered intensity as a function of the wave vector transfer, q orientation in the ring, α (Fig. 5a) which is also the orientation of the normal to the smectic layers (Fig. 2b). Intensity and q values as a function of α were determined from a fit of the diffraction data to a Gaussian function. To fulfill the Bragg condition and to ensure a broad coverage of α range, we have measured the scattering ring for various incident angles ω (Fig. 5a), i.e. ω = 0.15° and ω = 0.6°.

Indeed, ω = 0.6° is the Bragg angle for 8CB smectic layers: $\omega_B =$

$\arcsin\left(\frac{\lambda_0}{2d_0}\right) \approx 0.6°$ (where λ_0 is the X-ray wavelength, $\lambda_0 = 0.067$nm). The overall ring intensity is thus in Bragg condition for $\omega = \omega_B$, but α values smaller than $\arcsin\left(\frac{d_0}{\lambda_0}\sin(\omega)\right) \approx 29°$ are not reachable due to shadowing effects. Multiple scattering effects appearing at low q$_z$ values even further limit the minimum α value to around 40° For ω = 0.15°, α values as small as 15° can be attained, but Bragg conditions are only obtained for α < 70°. Combination of the ring intensities obtained with ω = 0.15° and with ω = 0.6° thus allows us to obtain the q curve of Fig. 3b and the curve of integrated intensity of Fig. 6 in Bragg condition. To explore the entire structure of the ring including the structure around α = 90° that comes from the top of the scattered ring, data with a displaced detector have been collected. This means that we both localized the dead area of the detector (in pink in Figs. 3a and 6) around the top of the ring (Fig. 3a) but also elsewhere than around the top of the ring (see Fig. 6).

In the transmission geometry (Fig. 5b), the sample is rotated by 90 ° around the Oy axis and the observed stripes become perpendicular to the incident beam. A local area of 300 μm × 100 μm is probed. The scattered signal shows two bracket-like scattering features associated with the sublayer of the smectic layers perpendicular to the rubbed direction and perpendicular to the substrate. Through a rotation around the axis Ox shown in Fig. 6b, the scattering as a function ofα can be probed up to α≈ 12° As a result, the almost complete q curve in Bragg condition as a function ofα is shown in Fig. 3b The scattered ring being symmetric like the SFHs, only values between 0° and 90° are shown.

5. Materials and Methods 2: Theoretical modelling

5.1. Order parameter

The orientational order is described by the traceless and symmetric nematic tensor order parameter [20,32]

$$\boldsymbol{Q} = \sum_{i=1}^{3} s_i \boldsymbol{e}_i \otimes \boldsymbol{e}_i, \tag{5}$$

where s_i are $\boldsymbol{Q}$ eigenvalues (*amplitude* fields), and $\boldsymbol{e}_i$ its normalised eigenvectors (*phase* fields). Note, that in general the *amplitude* phase space is two-dimensional due to the constraint $Tr\boldsymbol{Q} = \sum_{i=1}^{3} s_i = 0$.

In the case of uniaxial order, where two eigenvalues are equal, and $\boldsymbol{Q}$ is commonly expressed as [5]

$$\boldsymbol{Q} = s(\boldsymbol{n} \otimes \boldsymbol{n} - \boldsymbol{I}/3). \tag{6}$$

In this case $\boldsymbol{n}$ represents the principal $\boldsymbol{Q}$ eigenvector $\boldsymbol{e}_1$, and the
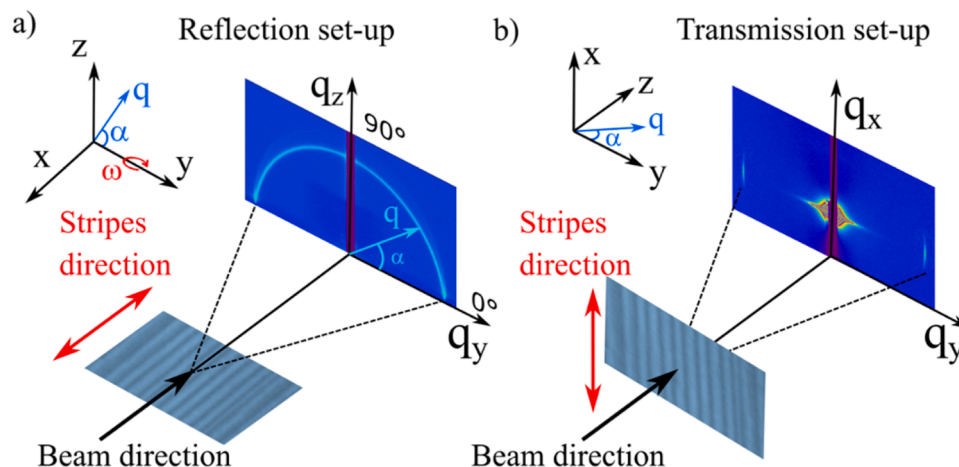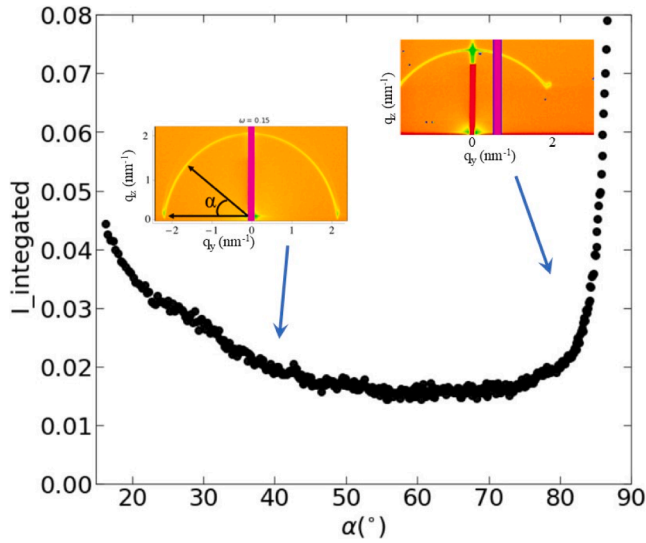

Fig. 5. X-ray diffraction set-ups with images of the measured signals on the EIGER 1 M detector: (a) Grazing incidence reflection set-up, showing the LC scattering ring. (b) Transmission set-up, showing two bracket-like scattering features perpendicular to the stripes.

Fig. 6. Intensity as a function of α, extracted from the combination of the ring obtained at ω = 0.15° and at ω = 0.6°. Two rings with different localization of the dead zone (in pink) have been used to allow for a broad observation of the scattered ring, including the top zone around α = 90°.
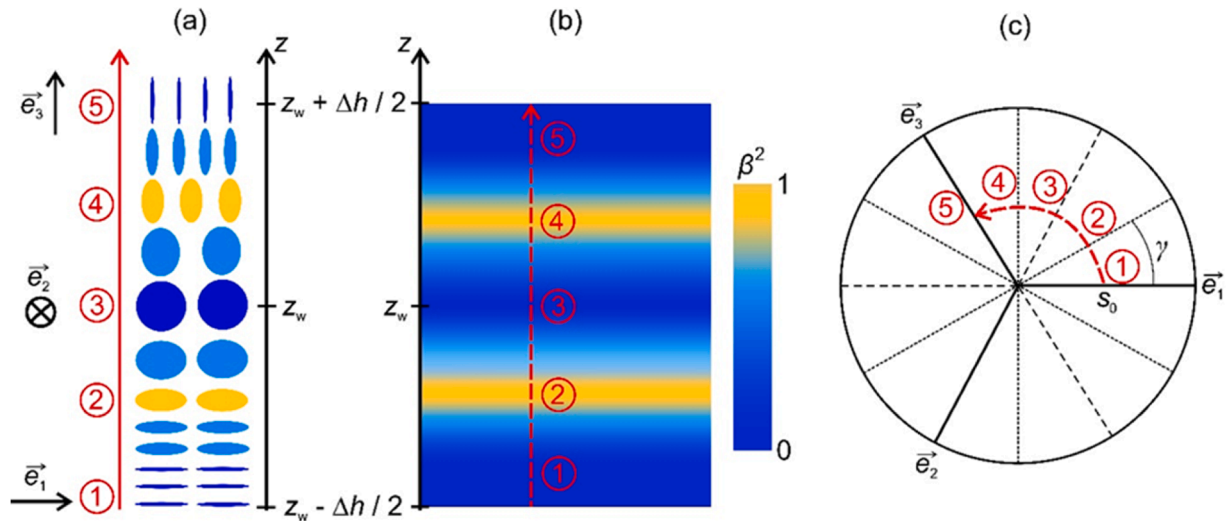
corresponding eigenvalue reads $s = \frac{3}{2}\textbf{n}.\textbf{Qn}$.

A convenient parametrisation of eigenvalues is given by 2D *amplitude phase space* [20,22] expressed by an angle γ and "radius" (effective amplitude) s_0:

$$s_1 = \frac{2s_0}{3}\cos\gamma, \ s_2 = -\frac{2s_0}{3}\cos\left(\gamma-\frac{\pi}{3}\right), \ s_3 = -\frac{2s_0}{3}\cos\left(\gamma+\frac{\pi}{3}\right), \tag{7a}$$

$$s_0 = \sqrt{\frac{3}{2}Tr\textbf{Q}^2}. \tag{7b}$$

Possible uniaxial and biaxial nematic states on varying s_0 and γ are depicted in Fig. 7c with respect to a fixed **Q** eigen-frame {e_1,e_2,e_3}. The melted isotropic state refers to the centre of the frame (i.e., $s_0 = 0$). Configurations determined by $\gamma = 0, \gamma = -\frac{2\pi}{3}$, and $\gamma = \frac{2\pi}{3}$ correspond to positive uniaxial states (i.e., $s > 0$ in Eq. (6)), where $\textbf{n} = e_1$, $\textbf{n} = e_2$, and $\textbf{n}$

= e_3, respectively. Values γ = π, γ = π/3, and γ = −π/3 refer to negative uniaxial states ($s < 0$), and $\textbf{n} = e_1$, $\textbf{n} = e_2$, and $\textbf{n} = e_3$, respectively. The degree of biaxiality attains its maximum ($\beta^2 = 1$) for γ = ±π/6, γ = ±π/2, and γ = ±5π/6.

For the latter analysis let us consider the case where the **Q** eigen frame (Eq. (5)) is allowed to rotate for an angle φ in the (y,z) plane of the Cartezian system, which is determined by unit vectors {e_x,e_y,e_z}, where

$$e_1 = \cos\varphi \ e_y + \sin\varphi \ e_z, \ e_2 = e_x, \ e_3 = -\sin\varphi \ e_y + \cos\varphi \ e_z. \tag{8}$$

Using parametrization given by Eqs. (7) and Eq. (8), representative qualitatively different nematic uniaxial and biaxial structures, where eigenvectors are allowed to rotate in (y,z) plane, could be expressed using only the pair of angles {φ, γ} and s_0, which quantifies effective amplitude of nematic order. For example, using **Q** parametrization given by Eqs. (7)-(8), the structural transformation in Fig. 1a is realised only by varying φ (i.e., in the case of equal nematic elastic constants it holds $\varphi = \frac{\pi}{2}\frac{z}{h}$). Furthermore, the imposed frustration could be resolved via order reconstruction, where φ = 0, see Fig. 7. In this case γ monotonously increases from γ(z = 0) to $\gamma(z = h) = \frac{3\pi}{2}$, enabling continuous transformation between positive uniaxial states $\textbf{n}(z = 0) = e_y$ and $\textbf{n}(z = h) = e_z$.

The SmA translational order is commonly described by the complex order parameter field [5,33]

$$\psi = \eta e^{i\phi}, \tag{9}$$

where η and φ represent the translational amplitude and symmetry-breaking field, respectively. This order parameter field approximately describes the mass density spatial variation ρ = $\rho_0(1 + \psi + \psi^*)$, where ρ_0 is a constant. In bulk equilibrium η is spatially homogeneous,

$$\phi(\textbf{r}) = q_0\textbf{n} \cdot \textbf{r}, \tag{10}$$

where the smectic layers are stacked along the symmetry breaking direction **n** with the periodicity $q_0 = 2\pi/d_0$. Here d_0 determines the equilibrium smectic layer spacing.

5.2. Free energy

In terms of nematic and smectic order parameters, we write the free energy density as the sum $f = f_c^{(n)} + f_e^{(n)} + f_c^{(s)} + f_e^{(s)} + f_{cp}$ of nematic

Fig. 7. a) Schematic geometric presentation of nematic order changes in the OR transformation when system's orientational order is forced to change on a relatively short distance Δh ∼ ξ_b. The centre of the OR deformation is placed at z = z_w. States labelled by (1,5) exhibiting positive uniaxial order, (3) negative uniaxial order, and (2,4) display maximal biaxiality. b) Spatial variation of the biaxiality parameter β^2. c) The OR transformation shown in the amplitude order parameter space in the Lyuksyutov approximation. 1: γ=0, positive uniaxiality; 2: γ = π/6, maximal biaxiality; 3: γ = π/3, negative uniaxiality; 4: γ = π/2, maximal biaxiality; 5: γ = 2π/3, positive uniaxiality.

condensation $(f_c^{(n)})$, smectic condensation $(f_c^{(s)})$, nematic elastic $(f_e^{(n)})$, smectic elastic $(f_e^{(s)})$, and the term f_{cp} describing the coupling between the smectic and nematic order parameter. We express them as follows [5,20,33]

$$f_c^{(n)} = a_n(T - T_n^*)Tr\boldsymbol{Q}^2 - b_nTr\boldsymbol{Q}^3 + c_n(Tr\boldsymbol{Q}^2)^2, \tag{11a}$$

$$f_e^{(n)} = L|\nabla\boldsymbol{Q}|^2, \tag{11b}$$

$$f_c^{(s)} = a_s(T - T_s^*)|\psi|^2 + b_s|\psi|^4, \tag{11c}$$

$$f_e^{(s)} = C_\parallel|(iq_0\boldsymbol{e} - \nabla)\psi|^2 + C_\perp|(\boldsymbol{e} \times \nabla)\psi|^2, \tag{11d}$$

$$f_{cp} = -D\nabla\psi^*.\boldsymbol{Q}\nabla\psi. \tag{11e}$$

The Landau expansion coefficients a_n, b_n, c_n, a_s, b_s are assumed to be positive and temperature-independent, constants T_n^* and T_s^* are related (and are comparable) to the critical temperatures below which the orientational and translational order condensate, respectively. The nematic elastic LC properties are described by the representative nematic bare (i.e. temperature independent) elastic constant L, corresponding to the approximation of equal Frank elastic constant K (i.e., $K_{11} = K_{22} = K_{33} = K_{24} \equiv K \sim Ls^2$) in the Frank-Oseen uniaxial model [6]. The smectic elasticity is described by the compressibility ($C_\parallel$) and smectic bend ($C_\perp$) elastic constants, which are positive in the SmA phase. They enforce stacking of layers along the principal eigenvector $\boldsymbol{e}$ of the nematic order parameter $\boldsymbol{Q}$ with the layer spacing $d_0 = \frac{2\pi}{q_0}$. The positive coupling constant D quantifies the coupling strength between the orientational and translational LC order.

5.3. Lyuksyutov constraint

Key qualitative features of an order-reconstruction transformation could be relatively simply illustrated by exploiting the Lyuksyutov approximation (i.e., constraint). This approximation exploits the weakly first order character of the I-N phase transition. It assumes that i) amplitude of nematic ordering is dominantly influenced by the nematic condensation contribution $f_c^{(n)}$, and that ii) the cubic term (which is responsible for the 1st order character) plays a secondary role. Consequently, $f_c^{(n)} \approx a_n(T - T_n^*)Tr\boldsymbol{Q}^2 + c_nTr(\boldsymbol{Q}^2)^2$, which is minimized for

$$Tr\boldsymbol{Q}^2 = \frac{a_n(T_n^* - T)}{2c_n} = \frac{2s_0^2}{3}. \tag{12}$$

In the Lyuksyutov approximation we consider Eq. (12) as a constraint for $Tr\boldsymbol{Q}^2$. Consequently, γ is the only free variational parameter in the amplitude order parameter space. This approximation is sensible deep in the nematic phase.

5.4. Scaled free energy density

In the following, we parametrize nematic and smectic order parameters using Eqs. (8)-(10), and we adopt the Lyuksyutov constraint (Eq. (12)). For sake of simplicity, we neglect the anisotropy of smectic elastic constants, i.e., $C \equiv C_\parallel \sim C_\perp$. We also discard the coupling term. Consequently, our system exhibits a 2nd order nematic-smectic phase transition, taking place at the critical temperature $T_{NA} = T_s^*$. We introduce the scaled smectic order parameter [33] $\widetilde{\psi} = \widetilde{\eta}e^{i\phi}$, $\widetilde{\eta} = \frac{\eta}{\eta_0}$. Here $\eta_0 = \sqrt{a_sT_{NA}/(2b_s)}$ stands for the saturated smectic amplitude (i.e., $\widetilde{\eta} \leq 1$). We furthermore introduce the reduced temperature $r = \frac{T - T_{NA}}{T_{NA}}$ and several material dependent characteristic lengths. These are the nematic biaxial length [5,34] ξ_b, smectic order parameter correlation length ξ_s and smectic penetration length λ [5,33] We express them at relatively low temperatures, and define them as

$$\xi_b = \sqrt{2L/(3b_ns_0)}, \;\; \xi_s = \sqrt{C/(a_sT_{NA})}, \;\; \lambda = \sqrt{Ls_0^2/(C\eta_0^2q_0^2)}. \tag{13}$$

With this in mind we express the free energy densities as

$$\frac{f_c^{(n)}}{Ls_0^2} = \frac{4}{27\xi_b^2}(1 - \cos(3\gamma)), \tag{14a}$$

$$\frac{f_e^{(n)}}{Ls_0^2} = \frac{8}{3}\left(\frac{1}{4}|\nabla\gamma|^2 + \sin^2(\gamma - \pi/3)|\nabla\varphi|^2\right), \tag{14b}$$

$$\frac{f_c^{(s)}}{C\eta_0^2} = \frac{1}{\xi_s^2}\left(-r\,\widetilde{\eta}^2 + \frac{\widetilde{\eta}^4}{2}\right), \tag{14c}$$

$$\frac{f_e^{(s)}}{C\eta_0^2} = |(iq_0\boldsymbol{e} - \nabla)\widetilde{\psi}|^2 + |(\boldsymbol{e} \times \nabla)\widetilde{\psi}|^2. \tag{14d}$$

Note that within the Lyuksyutov constraint the nematic condensation term penalizes only biaxial states with respect to uniaxial ones (i.e., melting of nematic order is not allowed).

5.5. Classical nematic OR transformation

A detailed one dimensional nematic OR structural transformation mediating enforced mutually perpendicular uniaxial order at $z = z_w - \Delta h/2$ and $z = z_w + \Delta h/2$ along the z-direction of the Cartesian coordinates $\{\boldsymbol{e}_x, \boldsymbol{e}_z, \boldsymbol{e}_z\}$ is shown in Fig. 7. We impose $\boldsymbol{n}(z_w - \frac{\Delta h}{2}) = \boldsymbol{e}_1$ and $\boldsymbol{n}(z_w - \frac{\Delta h}{2}) = \boldsymbol{e}_3$ on a distance $\Delta h \sim \xi_b$, where $\{\boldsymbol{e}_1, \boldsymbol{e}_2, \boldsymbol{e}_3\} = \{\boldsymbol{e}_x, \boldsymbol{e}_y, \boldsymbol{e}_z\}$. In between $\boldsymbol{Q}$ enters biaxial states and the crosses state with negative uniaxial order along $\boldsymbol{e}_2$ at z_w. The structural transformation is realized by the exchange of $\boldsymbol{Q}$ eigenvalues and the $\boldsymbol{Q}$ eigenvector frame remains fixed. In Fig. 7a we show the mesoscopic geometrical changes on crossing the OR wall at z$_w$. The related variations in the degree of biaxiality β^2 are plotted in Fig. 7b Variations in two-dimensional *amplitude* order parameter space (see Eqs. (7)) are shown in Fig. 7c.

5.6. TWD stability conditions

Below we present some rough estimates concerning the TDW existence and stability. The OR mechanism is activated when large enough frustration in orientational order is imposed on the scale comparable to a nematic order parameter on a relatively short length scale. In our case we impose mutually perpendicular essentially uniaxial orientations over few smectic layer thicknesses. The corresponding elastic penalty in this deformation is approximately given by $L|\nabla\boldsymbol{Q}|^2 \sim Lq^2/\xi_d^2$, where q estimates a relevant effective amplitude of orientational order and ξ_d is the length scale across this deformation is realised. This elastic penalty competes with the cubic condensation term $b_nTr\boldsymbol{Q}^3 \sim b_nq^3$ (which resist the system to enter biaxial states) in the condensation free energy if local melting is relatively costly (i.e., the system is deep in the nematic phase). By equating these competing free energy contributions, it follows $\xi_d \sim \sqrt{L/(b_nq)}$, i.e., $\xi_d \sim \xi_b$ (see Eq. (13)). Note that such a frustration could be sustained only if strong enough anchoring stabilizes the conflicting boundary conditions. To estimate the required anchoring strength, we estimate the free energy cost of structures where the boundary conditions are not ($F = F_1$) and strictly ($F = F_2$) obeyed. In the 1st case the system exhibits a spatially homogeneous structure, and the resulting free energy penalty arises due to anchoring condition violation. It roughly holds $F_1 \sim A\xi_bw$, where w stands for the representative anchoring strength and A is the surface area. In the second case only the elastic free energy penalty is present, i.e. $F_2 \sim \frac{ALq^2}{\xi_b}$. From the condition $F_1 \sim F_2$ it follows $\xi_b \sim d_e$, where $d_e \sim Lq^2/w$ stands for the surface extrapolation length. For $\xi_b \sim 10$ nm and $Lq^2 \sim 10^{-11}$ J/m we obtain $w \sim 10^{-3}$ J/m^2.

Finally, we estimate the effective anchoring strength of the defect

wall. For this purpose we focus on the smectic layer just above (or below) the melted wall region which favor parallel alignment of $\boldsymbol{n}$ and the local smectic layer normal $\boldsymbol{v}$. The smectic layers enforce $\theta = ArcCos$ $(\boldsymbol{n}.\boldsymbol{v}) \rightarrow 0$ via the smectic-bend free energy compression density term, whose quadratic expansion in θ reads $f_{e,\perp}^{(s)} \sim C_{\perp} q_0^2 \eta^2 \theta^2 = \frac{\theta^2 K}{\lambda^2}$, where $K \sim Lq^2$ is the representative Frank elastic constant. The corresponding free energy per surface area of one smectic layer reads $f_{e,\perp}^{(s)} d_0 \sim w\theta^2$, where $w = \frac{d_0 K}{\lambda^2}$ stands for the effective anchoring strength. For $d_0 \sim \lambda$ it follows $w \sim 10^{-2}$ J/m^2.

Funding sources

CRediT authorship contribution statement

Luka Mesarec: Writing – review & editing, Writing – original draft, Visualization, Validation, Software, Methodology, Investigation. **Jean de Dieu Niyonzima:** Writing – review & editing, Visualization, Methodology, Investigation. **Haifa Jeridi:** Writing – review & editing, Investigation. **Alina Vlad:** Writing – review & editing, Investigation. **Alessandro Coati:** Writing – review & editing, Investigation. **Michel Goldmann:** Writing – review & editing, Investigation. **David Babonneau:** Writing – review & editing, Investigation. **Doru Constantin:** Writing – review & editing, Investigation. **Yves Garreau:** Writing – review & editing, Methodology, Investigation. **Bernard Croset:** Writing – review & editing, Methodology. **Aleš Iglič:** Writing – review & editing, Supervision. **Emmanuelle Lacaze:** Writing – review & editing, Writing – original draft, Validation, Supervision, Methodology, Investigation, Conceptualization. **Samo Kralj:** Writing – review & editing, Writing – original draft, Validation, Supervision, Methodology, Conceptualization.

Declaration of competing interest

The authors declare the following financial interests/personal relationships which may be considered as potential competing interests:

Luka Mesarec reports financial support was provided by Slovenian Research Agency (ARIS). Ales Iglic reports financial support was provided by Slovenian Research Agency (ARIS). Samo Kralj reports was provided by Slovenian Research Agency (ARIS). Jean de Dieu Niyonzima reports financial support was provided by French embassy in Rwanda. If there are other authors, they declare that they have no known competing financial interests or personal relationships that could have appeared to influence the work reported in this paper.

Data availability

No data was used for the research described in the article.

References

[1] P.G. de Gennes, Soft Interfaces, Cambridge University Press, New York, 1997, https://doi.org/10.1017/CBO9780511628764.

[2] T.J. Sluckin, A. Poniewierski, Fluid Interfacial Phenomena, Wiley, Chichester, 1986.

[3] A.D. Rey, Thermodynamics of soft anisotropic interfaces, J. Chem. Phys. 120 (2004) 2010–2019, https://doi.org/10.1063/1.1635357.

[4] N.D. Mermin, The topological theory of defects in ordered media, Rev. Mod. Phys. 51 (1979) 591–648, https://doi.org/10.1103/RevModPhys.51.591.

[5] M. Kleman, O.D. Lavrentovich, Soft Matter Physics: An Introduction, Springer-Verlag, New York, 2004.

[6] P.G. de Gennes, J. Prost, The Physics of Liquid Crystals, 2nd ed., Clarendon Press, Oxford, 1994.

[7] O.D. Lavrentovich, Topological defects in dispersed liquid crystals, or words and worlds around liquid crystal drops, Liq. Cryst. 24 (1998) 117–125, https://doi.org/10.1080/026782998207640.

[8] P. Palffy-Muhoray, E.C. Gartland, J.R. Kelly, A new configurational transition in inhomogeneous nematics, Liq. Cryst. 16 (1994) 713–718, https://doi.org/10.1080/02678299408036543.

[9] G. Lombardo, A. Amoddeo, R. Hamdi, H. Ayeb, R. Barberi, Biaxial surface order dynamics in calamitic nematics, Eur. Phys. J. E 35 (2012) 32, https://doi.org/10.1140/epje/i2012-12032-y.

[10] F. Bisi, E.C. Gartland, R. Rosso, E.G. Virga, Order reconstruction in frustrated nematic twist cells, Phys. Rev. E 68 (2003) 021707, https://doi.org/10.1103/PhysRevE.68.021707.

[11] N. Schopohl, T.J. Sluckin, Defect core structure in nematic liquid crystals, Phys. Rev. Lett. 59 (1987) 2582–2584, https://doi.org/10.1103/PhysRevLett.59.2582.

[12] C.E. Williams, M. Kléman, Dislocations, grain boundaries and focal conics in smectics A, J. Phys. France 36 (1975). C1-315–C1-319, https://hal.science/jpa-00216231v1.

[13] C. Blanc, M. Kleman, Curvature walls and focal conic domains in a lyotropic lamellar phase, Eur. Phys. J. B 10 (1999) 53–58, https://doi.org/10.1007/s100510050829.

[14] D. Coursault, B. Zappone, A. Coati, A. Boulaoued, L. Pelliser, D. Limagne, N. Boudet, B. Haj Ibrahim, A. de Martino, M. Alba, M. Goldmann, Y. Garreau, B. Gallas, E. Lacaze, Self-organized arrays of dislocations in thin smectic A films, Soft. Matter 12 (2016) 678–688, https://doi.org/10.1039/C5SM02241J.

[15] J.P. Michel, E. Lacaze, M. Alba, M. de Boissieu, M. Gailhanou, M. Goldmann, Optical gratings formed in thin smectic films frustrated on a single crystalline substrate, Phys. Rev. E 70 (2004) 011709, https://doi.org/10.1103/PhysRevE.70.011709.

[16] D. Coursault, B. Haj Ibrahim, L. Pelliser, B. Zappone, A. de Martino, E. Lacaze, B. Gallas, Modeling the optical properties of self-organized arrays of liquid crystal defects, Opt. Express 22 (2014) 23182–23191, https://doi.org/10.1364/OE.22.023182.

[17] A.J. Leadbetter, J.C. Frost, J.P. Gaughan, G.W. Gray, A. Mosley, The structure of smectic A phases of compounds with cyano end groups, J. Phys. 40 (1979) 375–380, https://doi.org/10.1051/jphys:01979004004037500.

[18] N.A. Clark, T. Bellini, R.M. Malzbender, B.N. Thomas, A.G. Rappaport, D. W. Schaefer, C.W. Garland, X-ray scattering study of smectic ordering in a silica aerogel, Phys. Rev. Lett. 71 (1993) 3505–3508, https://doi.org/10.1103/PhysRevLett.71.3505.

[19] P. Kaiser, W. Wiese, S. Hess, Stability and instability of a uniaxial alignment against biaxial distortions in the isotropic and nematic phases of liquid crystals, J. Non-Equilib. Thermodyn. 17 (1992) 153–169, https://doi.org/10.1515/jnet.1992.17.2.153.

[20] S. Kralj, R. Rosso, E.G. Virga, Finite-size effects on order reconstruction around nematic defects, Phys. Rev. E 81 (2010) 021702, https://doi.org/10.1103/PhysRevE.81.021702.

[21] J. Xia, S. MacLachlan, T.J. Atherton, P.E. Farrell, Structural landscapes in geometrically frustrated smectics, Phys. Rev. Lett. 126 (2021) 177801, https://doi.org/10.1103/PhysRevLett.126.177801.

[22] J. Kralj, E.G. Virga, S. Žumer, Biaxial torus around nematic point defects, Phys. Rev. E 60 (1999) 1858–1866, https://doi.org/10.1103/PhysRevE.60.1858.

[23] I.F. Lyuksyutov, Topological instability of singularities at small distances, Zh. Eksp. Teor. Fiz. 75 (1978) 358–360.

[24] S. Kralj, T.J. Sluckin, Landau–de Gennes theory of the core structure of a screw dislocation in smectic A liquid crystals, Liq. Cryst. 18 (1995) 887–902, https://doi.org/10.1080/02678299508036707.

[25] M. Ambrožič, S. Kralj, E.G. Virga, Defect-enhanced nematic surface order reconstruction, Phys. Rev. E 75 (2007) 031708, https://doi.org/10.1103/PhysRevE.75.031708.

[26] F. Ciuchi, H. Ayeb, G. Lombardo, R. Barberi, G.E. Durand, Control of transient biaxial order in calamitic nematics, Appl. Phys. Lett. 91 (2007) 24, https://doi.org/10.1063/1.2824830.

[27] H. Kikuchi, M. Yokota, Y. Hisakado, T. Kajiyama, Polymer-stabilized liquid-crystals blue phases, Nat. Mater. 1 (2002) 64, https://doi.org/10.1038/nmat712.

[28] E. Karatairi, et al., Nanoparticle-induced widening of the temperature range of liquid-crystalline blue phases, Phys. Rev. E 81 (2010) 041703, https://doi.org/10.1103/PhysRevE.81.041703.

[29] D. Coursault, et al., Linear self-assembly of nanoparticles within liquid crystal defect arrays, Adv. Mater. 24 (2012) 1461, https://doi.org/10.1002/adma.201103791.

[30] S.-P. Do, A. Missaoui, A. Coati, D. Coursault, H. Jeridi, A. Resta, N. Goubet, M. M. Wojcik, A. Choux, S. Royer, E. Briand, B. Donnio, J.L. Gallani, B. Pansu, E. Lhuillier, Y. Garreau, D. Babonneau, M. Goldmann, D. Constantin, B. Gallas, B. Croset, E. Lacaze, From chains to monolayers: nanoparticle assembly driven by smectic topological defects, Nano Lett. 20 (2020) 1598–1606, https://doi.org/10.1021/acs.nanolett.9b04347.

[31] H. Jeridi, J.D. Niyonzima, A. Missaoui, S. Shahini, A. Vlad, A. Coati, N. Goubet, S. Royer, I. Vickridge, M. Goldmann, D. Constantin, Y. Garreau, D. Babonneau, B. Croset, B. Gallas, E. Lhuillier, E. Lacaze, Unique orientation of 1D and 2D nanoparticle assemblies confined in smectic topological defects, Soft. Matter 18 (2022) 4792–4802, https://doi.org/10.1039/D2SM00376G.

[32] R. Rosso, E.G. Virga, Metastable nematic hedgehogs, J. Phys. A: Math. Gen. 29 (1996) 4247, https://doi.org/10.1088/0305-4470/29/14/041.

[33] S. Kralj, T.J. Sluckin, Core structure of a screw disclination in smectic A liquid crystals, Phys. Rev. E 49 (1993) R3244–R3247, https://doi.org/10.1103/PhysRevE.48.R3244.

[34] F. Bisi, E.C. Gartland Jr., R. Rosso, E.G. Virga, Order reconstruction in frustrated nematic twist cells, Phys. Rev. E 68 (2003) 021707, https://doi.org/10.1103/PhysRevE.68.021707.